

Physical conditions in the neutral interstellar medium at $z = 2.43$ toward Q 2348–011[★]

P. Noterdaeme¹, P. Petitjean^{2,3}, R. Srianand⁴, C. Ledoux¹, and F. Le Petit⁵

¹ European Southern Observatory, Alonso de Córdova 3107, Casilla 19001, Vitacura, Santiago, Chile
e-mail: [pnoterda; cledoux]@eso.org

² Institut d’Astrophysique de Paris, CNRS - Université Pierre et Marie Curie, 98bis boulevard Arago, 75014 Paris, France
e-mail: petitjean@iap.fr

³ LERMA, Observatoire de Paris, 61 avenue de l’Observatoire, 75014 Paris, France

⁴ IUCAA, Post Bag 4, Ganesh Khind, Pune 411 007, India
e-mail: anand@iucaa.ernet.in

⁵ LUTH, Observatoire de Paris, 61 Avenue de l’Observatoire, 75014 Paris, France
e-mail: franck.1epetit@obspm.fr

Received 7 December 2006 / Accepted 6 March 2007

ABSTRACT

Aims. We aim at deriving the physical conditions in the neutral gas associated with damped Lyman- α systems using observation and analysis of H₂ and C I absorptions.

Methods. We obtained a high-resolution VLT-UVES spectrum of the quasar Q 2348–011 over a wavelength range that covers most of the prominent metal and molecular absorption lines from the $\log N(\mathrm{H}\,\mathrm{I}) = 20.50 \pm 0.10$ damped Lyman- α system at $z_{\mathrm{abs}} = 2.4263$. We detected H₂ in this system and measured column densities of H₂, C I, C I^{*}, C I^{**}, Si II, P II, S II, Fe II, and Ni II. From the column density ratios and, in particular, the relative populations of H₂ rotational and C I fine-structure levels, we derived the physical conditions in the gas (relative abundances, dust-depletion, particle density, kinetic temperature, and ionising flux) and discuss physical conditions in the neutral phase.

Results. Molecular hydrogen was detected in seven components in the first four rotational levels ($J = 0$ –3) of the vibrational ground state. Absorption lines of H₂ $J = 4$ (resp. $J = 5$) rotational levels are detected in six (resp. two) of these components. This leads to a total molecular fraction of $\log f \simeq -1.69_{-0.58}^{+0.37}$. Fourteen components are needed to reproduce the metal-line profiles. The overall metallicity is found to be -0.80 , -0.62 , -1.17 ± 0.10 for, respectively, [Si/H], [S/H] and [Fe/H]. We confirm the earlier findings that there is a correlation between $\log N(\mathrm{Fe}\,\mathrm{II})/N(\mathrm{S}\,\mathrm{II})$ and $\log N(\mathrm{Si}\,\mathrm{II})/N(\mathrm{S}\,\mathrm{II})$ from different components indicative of a dust-depletion pattern. Surprisingly, however, the depletion of metals onto dust in the H₂ components is not large in this system: [Fe/S] = -0.8 to -0.1 .

The gas in H₂-bearing components is found to be cold but still hotter than similar gas in our Galaxy ($T > 130$ K, instead of typically 80 K) and dense ($n \sim 100$ –200 cm⁻³). There is an anti-correlation ($R = -0.97$) between the logarithm of the photo-absorption rate, $\log \beta_0$, and $\log N(\mathrm{H}_2)/N(\mathrm{C}\,\mathrm{I})$ derived for each H₂ component. We show that this is mostly due to shielding effects and imply that the photo-absorption rate β_0 is a good indicator of the physical conditions in the gas. We find that the gas is immersed in an intense UV field, about one order of magnitude higher than in the solar vicinity. These results suggest that the gas in H₂-bearing DLAs is clumpy, and star-formation occurs in the associated object.

Key words. galaxies: ISM – quasars: absorption lines – quasars: individuals: Q 2348–011

1. Introduction

High-redshift damped Lyman- α systems (DLAs) detected in absorption in QSO spectra are characterised by their large neutral hydrogen column densities, $N(\mathrm{H}\,\mathrm{I}) \geq 2 \times 10^{20}$ cm⁻², similar to what is measured through local spiral disks (Wolfe et al. 1986). The corresponding absorbing clouds are believed to be the reservoir of neutral hydrogen in the Universe (e.g., Péroux et al. 2003; Prochaska et al. 2005). Though observational studies of DLAs have been pursued over more than two decades (see Wolfe et al. 2005, for a recent review), important questions are still unanswered, such as (i) the amount of in-situ star-formation activity in DLAs, (ii) the connection between observed abundance ratios

and the dust content, and (iii) how severe is the bias due to dust obscuration in current DLA samples.

One way to tackle these questions is to derive the physical conditions that prevail in the absorbing gas by studying the excitation of molecular and atomic species together. Since UV-lines are redshifted into the optical, a single VLT-UVES spectrum allows one to simultaneously observe a large number of absorption lines of important species at high spectral resolution and with a good signal-to-noise ratio. In the case of the Galactic interstellar medium (ISM), only a few lines of sight have been observed in such detail.

Although molecular hydrogen is the most abundant molecule in the Universe, it is very difficult to detect directly. The molecule has a rich absorption spectrum in the UV, and space-crafts have been used to detect the absorption lines from clouds located in our Galaxy in front of bright background stars. At H I column densities as high as those measured in DLAs or

[★] Based on observations carried out at the European Southern Observatory (ESO) under prog. ID No. 072.A-0346 with the UVES spectrograph installed at the Very Large Telescope (VLT) Unit 2, Kueyen, on Cerro Paranal, Chile.

sub-DLAs ($N(\text{H I}) > 19.5 \text{ cm}^{-2}$), H_2 molecules are conspicuous in our Galaxy: sightlines with $\log N(\text{H I}) > 21$ usually have $\log N(\text{H}_2) > 19$ (see Savage et al. 1977; Jenkins & Shaya 1979). More recently, observations with the Far Ultraviolet Spectroscopic Explorer (FUSE) have derived the physical conditions in the diffuse molecular gas in the Galaxy but also the Magellanic clouds (Tumlinson et al. 2002) or high Galactic latitude lines of sight (Richter et al. 2003; Wakker 2006). In the Magellanic clouds, molecular fractions and kinetic temperatures are reported to be, respectively, lower and higher than in the local ISM. This is probably a consequence of higher UV ambient flux and lower dust content. In intermediate velocity clouds located in the Galactic halo, H_2 is found to arise in cold ($T \lesssim 140 \text{ K}$), dense ($n_{\text{H}} \sim 30 \text{ cm}^{-3}$), and clumpy ($D \sim 0.1 \text{ pc}$) clouds (Richter et al. 2003), embedded in a relatively low UV flux.

At high redshift, UV-lines are redshifted in the optical so ground-based telescopes can be used. Quasars (e.g., Levshakov et al. 1992; Ge & Bechtold 1999; Ledoux et al. 2003) but also recently γ -ray burst afterglows (Fynbo et al. 2006) are used as background sources. The amount of H_2 molecules seen in DLAs is much less than what is observed in our Galaxy. Ledoux et al. (2003) find that about 15% of DLAs show detectable H_2 with molecular fraction in the range $-4 < \log f < -1$. This fraction increases with metallicity and reaches 50% for $[\text{X}/\text{H}] > -0.7$ (Petitjean et al. 2006). The fact that H_2 is less conspicuous at high redshift can be explained as a consequence of lower metal content and therefore lower dust content, together with higher ambient UV flux. It could be also that the covering factor of the diffuse molecular gas is low.

Detailed analysis of H_2 -bearing DLAs has been pursued in some cases. Cui et al. (2005) recently derived a surprisingly low hydrogen density, $n_{\text{H}} \approx 0.2 \text{ cm}^{-3}$, using $R \sim 30\,000$ STIS data from the HST, and an electron temperature of $T_{\text{e}} \approx 140 \text{ K}$ in the H_2 system at $z_{\text{abs}} = 1.776$ toward Q 1331+170. Other authors, however, usually derive higher densities. By studying the spectrum of the $z_{\text{abs}} \approx 2.811$ DLA toward PKS 0528–250, Srianand & Petitjean (1998) derived a kinetic temperature of $T \sim 200 \text{ K}$ and a density of $n \sim 1000 \text{ cm}^{-3}$. They suggest that the ratio $N(\text{H}_2)/N(\text{C I})$ could be a good indicator of the physical conditions in the gas. Petitjean et al. (2002) derived gas pressure, particle density, excitation temperatures, and ambient UV fluxes for four H_2 components at $z_{\text{abs}} \approx 1.973$ toward Q 0013–004. They show that, whenever H_2 is detected, the particle density is high ($n_{\text{H}} \sim 30\text{--}200 \text{ cm}^{-3}$) and the kinetic temperature is low ($T \sim 100 \text{ K}$). In addition, the ambient UV radiation field is found to be highly inhomogeneous. Ledoux et al. (2002) find high particle densities ($n \sim 30\text{--}400 \text{ cm}^{-3}$) and moderate UV radiation field in a DLA at $z_{\text{abs}} = 1.962$. They conclude that physical conditions play an important role in governing the molecular fraction in DLAs. Reimers et al. (2003) also found a high particle density ($n \sim 100 \text{ cm}^{-3}$) in a DLA at $z_{\text{abs}} = 1.150$. From the high derived UV radiation field, they suggest there is ongoing star-formation activity close to the absorbing cloud. Srianand et al. (2005) use the 33 systems from the high-resolution ($R \sim 45\,000$) UVES survey by Ledoux et al. (2003) – among which 8 show detectable H_2 absorption lines – to compare observations and molecular cloud models. They conclude that the mean kinetic temperature in H_2 -bearing DLAs is higher ($\sim 150 \text{ K}$) than in the local ISM ($\sim 80 \text{ K}$), the UV flux is close to or higher than the mean UV flux in the ISM of the Galaxy, and the particle densities ($\sim 10\text{--}200 \text{ cm}^{-3}$) and photo-ionisation rate are similar to the ones in the Galactic cold neutral medium. More recently, gas temperature, $T \sim 90\text{--}180 \text{ K}$, and density, $n_{\text{H}} \leq 50 \text{ cm}^{-3}$, were derived in a DLA at $z_{\text{abs}} \approx 4.224$, which corresponds to the

highest redshift at which this kind of study has been done up to now (Ledoux et al. 2006b).

We recently reported the detection of H_2 in the $z_{\text{abs}} = 2.4263$ DLA toward Q 2348–011 (Petitjean et al. 2006). We present here a detailed analysis of the physical conditions in the gas. This system has one of the highest molecular fractions ever measured at high redshift, and seven H_2 components are detected in which physical conditions can be derived. This is the first time that a comparison of physical conditions can be made in such a large number of components in a single absorption system. The paper is organised as follows. In Sect. 2, we describe observations and data reduction. In Sect. 3, we give details on the data and present the fits to the H_2 , C I and low-ionisation metal absorption lines. In Sect. 4, we discuss the relative populations of H_2 rotational levels, and C I fine-structure levels, deriving information on the physical state of the gas. Finally, we discuss our findings and draw our conclusions in Sect. 5.

2. Observations

The quasar Q 2348–011 was observed with the Ultraviolet and Visible Echelle Spectrograph (UVES; Dekker et al. 2000) mounted on the ESO Kueyen VLT-UT2 8.2 m telescope on Cerro Paranal in Chile in visitor mode on October 29 and 30, 2003, under good seeing conditions ($FWHM < 0.8 \text{ arcsec}$) and at low airmass ($AM < 1.2$). Three 5400 s exposures were taken with Dichroic #1 simultaneously with the blue and red arms. We used a 1.0 arcsec slit width and a pixel binning of 2×2 , leading to a resolving power of $R \approx 47\,000$. The data were reduced using the UVES pipeline (Ballester et al. 2000), which is available in the context of the ESO MIDAS data reduction system. The main characteristics of the pipeline are to perform a precise inter-order background subtraction, especially for master flat fields, and to allow for an optimal extraction of the object signal rejecting cosmic rays and performing sky subtraction at the same time. The pipeline products were checked step-by-step.

The wavelength scale of the reduced spectra was then converted to vacuum-heliocentric values, and the portions of the spectrum corresponding to different arms were rebinned to a constant wavelength step. Individual 1D exposures were scaled, weighted, and combined. No other rebin was performed during the analysis of the whole spectrum. Standard Voigt-profile fitting methods were used for the analysis to determine column densities using the wavelengths and oscillator strengths compiled in Table 1 of Ledoux et al. (2003) for metal ions and the oscillator strengths given by Abgrall et al. (1993) for H_2 . We adopted the Solar abundances given by Morton (2003) based on the meteoritic data from Grevesse & Sauval (2002).

3. The DLA at $z_{\text{abs}} = 2.4263$ toward Q 2348–011

There are two DLAs at $z_{\text{abs}} = 2.42630$ and $z_{\text{abs}} = 2.61473$ toward Q 2348–011. These DLAs were discovered as strong Lyman- α absorptions in a low spectral-resolution ($\sim 5 \text{ \AA}$) spectrum by Sargent et al. (1989), who also observed strong metal lines associated to the $z_{\text{abs}} = 2.4263$ DLA. From Voigt-profile fitting to the damped Lyman- α line, we find that the total neutral hydrogen column density of the system at $z_{\text{abs}} = 2.4263$ is $\log N(\text{H I}) = 20.50 \pm 0.10$ (Ledoux et al. 2006a). A simultaneous Voigt-profile fitting of the Lyman- α and Lyman- β lines was also performed for the system at $z_{\text{abs}} = 2.6147$. Note that the $z_{\text{abs}} = 2.6147$ Lyman- β line falls in the wavelength range where H_2 lines at $z_{\text{abs}} = 2.4263$ are detected (see Fig. 1).

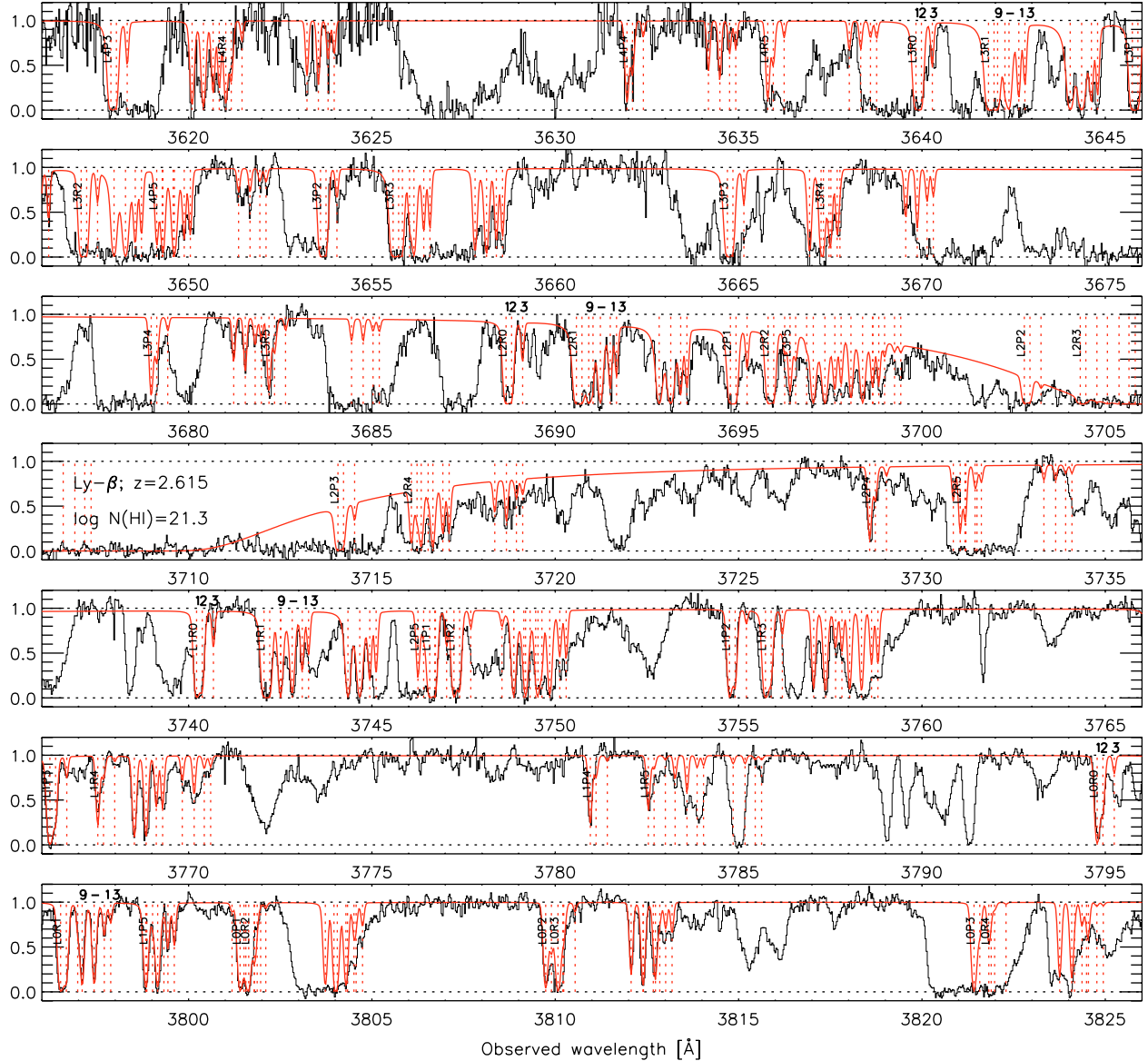


Fig. 1. A portion of the normalised spectrum of Q 2348–011. The resolving power is about $R \simeq 47\,000$. The H₂ spectrum derived from Voigt-profile fitting is superimposed to the quasar spectrum. The strong feature at $\lambda \simeq 3707$ Å is the Ly- β absorption line from the DLA at $z_{\text{abs}} = 2.6147$. H₂ components are numbered for the $J = 0$ rotational level only. Transition names are abbreviated as LxYz standing for H₂ Lx–0Yz, and only marked for component 1. The best fit parameters are given in Table 2.

The total neutral hydrogen column density for this system is $\log N(\text{H I}) = 21.30 \pm 0.08$ (Ledoux et al. 2006a). No molecular hydrogen is detected at this redshift down to $\log N(\text{H}_2) < 13.7$ (considering rotational levels $J = 0$ and $J = 1$), or $\log f < -7.2$.

3.1. Molecular content

The H₂ absorption lines at $z_{\text{abs}} = 2.4263$ are strong and numerous (see Fig. 1). Although they are all redshifted in the Lyman- α forest, the resolving power of our data ($R \simeq 47\,000$) is high enough to allow unambiguous detection and accurate determination of the line parameters.

3.1.1. Overall fit

The absorption profiles of the singly-ionised metal species have been fitted using fourteen components and, in the

following, we use their numbering to refer to any individual velocity component. Seven of these components, spread over about 300 km s^{-1} , show associated H_2 absorption. Multiple component Voigt-profile fittings have been performed simultaneously on the H_2 absorption lines seen redward of the Lyman break produced by the $z_{\text{abs}} = 2.6147$ system, also including the Voigt profile of the Ly- β line at $z_{\text{abs}} = 2.6147$. The continuum normalisation was performed using first-order broken lines between $\lambda_{\text{obs}} \simeq 3600 \text{ \AA}$ and $\lambda_{\text{obs}} \simeq 3850 \text{ \AA}$ and a routine based on the IRAF task *continuum* that can fit segments of $50\text{--}100 \text{ \AA}$ at once. For each $\sim 50 \text{ \AA}$ wavelength range, the continuum is fitted by approximately five to seven joint linear segments adjusted by an iterative procedure that rejects absorptions over a certain threshold related to the local signal-to-noise ratio. This allows us to estimate the continuum position where the Lyman- α forest is dense, and over the $z_{\text{abs}} = 2.6147$ Ly- β absorption (see Fig. 1). Note that only the H_2 Lyman band is covered by our spectrum.

Table 1. Transitions used to constrain H_2 column densities in the seven components.

Level	# 1 & 2	# 3	# 9 & 10	# 12	# 13
$J = 0$	L0R0		L0R0	L0R0	L0R0
	L1R0	L1R0	L1R0	L1R0	
	L2R0	L2R0	L2R0	L2R0	L2R0
$J = 1$	L0P1	L0P1			
	L0R1	L0R1	L0R1	L0R1	L0R1
	L1P1	L1P1	L1P1		
	L1R1		L1R1	L1R1	
	L2R1		L2R1	L2R1	
	L3P1	L3P1		L3R1	L3R1
$J = 2$	L0P2		L0P2	L0P2	L0P2
	L0R2	L0R2		L0R2 ^l	L0R2 ^l
	L1P2	L1P2	L1P2		L1P2 ^u
	L1R2			L1R2 ^l	L1R2 ^l
	L3P2	L3P2			L3R2 ^u
					L3R2 ^u
$J = 3$	L0R3	L0R3	L0R3 ^l	L0R3 ^l	
	L1P3	L1P3 ^u	L1P3	L1P3	L1P3 ^u
	L1R3	L1R3			
	L3R3			L3P3	L3P3
				L3R3 ^u	L3R3 ^u
				L4P3	L4P3
$J = 4$	L1P4	L1P4 ^u			
	L1R4	L1R4 ^u			
	L2P4			L3P4	L3P4
	L4P4	L4P4 ^u	L4P4	L4P4	L4P4
	L4R4	L4R4 ^u		L4R4	L4R4
$J = 5$	L1R5			L2R5 ^u	L2R5 ^u
	L3R5	L3R5 ^u			
				L4P5 ^u	L4P5 ^u
				L4P5 ^u	L4P5 ^u

Transition names are abbreviated as LxYz standing for H_2 Lx–0 Yz. “u” (resp. “l”) means that the transition is used to give an upper (resp. lower) limit on $N(\text{H}_2; J)$.

The solution of a multi-component Voigt-profile fit is often not unique, especially when absorption lines are blended and sometimes saturated. In that case, it is difficult to constrain both the Doppler parameters and the column densities at the same time for all species. We therefore obtained a first guess of the molecular parameters by fitting selected lines (see Table 1) of the first four rotational levels, $J = 0$ to $J = 3$, using Doppler parameters and redshifts derived from the C I profiles, which are not saturated and located outside the Lyman- α forest. We then froze the corresponding parameters and added the $J = 4$ and $J = 5$ features. After a satisfactory fit to all H_2 transitions had been found in these conditions, we relaxed all parameters one by one, until the best fit was obtained. Then, a range of column densities was derived by fitting the absorption features with the extreme values of the Doppler parameter (see Table 2). The errors given in Col. 4 of Table 2 therefore correspond to a range of column densities and not to the RMS errors derived from fitting the Voigt profiles. The quality of the overall fit can be assessed from Fig. 1 and in Figs. 9 to 14. Results are presented in Table 2. The total H_2 column density integrated over all rotational levels is $\log N(\text{H}_2) = 18.52^{+0.29}_{-0.49}$, corresponding to a molecular fraction $\log f = -1.69^{+0.37}_{-0.58}$. We also derive a 3σ upper limit on the column density of HD molecules, leading to $\log N(\text{HD})/N(\text{H}_2) < -3.3$ for the strongest H_2 components (# 1, 9 and 10). We describe individual components below.

Table 2. Voigt-profile fitting results for different rotational levels of the vibrational ground-state transition lines of H_2 .

#	z_{abs} $v^1 [\text{km s}^{-1}]$	Level	$\log N(\text{H}_2, J)^2$	b [km s^{-1}]	T_{0-J}^3 [K]
1	2.42449(7)	$J = 0$	15.55–17.40	$2.9^{+3.1}_{-0.4}$...
	–158	$J = 1$	16.40–18.00	“	183 $^{+145}_{-145}$
		$J = 2$	15.90–17.70	“	262 $^{+161}_{-161}$
		$J = 3$	16.10–17.80	“	510 $^{+340}_{-340}$
		$J = 4$	15.25–15.50	“	274 $^{+464}_{-35}$
		$J = 5$	14.90–15.20	“	311 $^{+283}_{-35}$
		$J = 6$	<14.00	“	≤ 584
		$J = 7$	<13.80	“	≤ 610
	2.42463(8)	$J = 0$	$15.35^{+0.10}_{-0.10}$	$3.5^{+1.0}_{-1.0}$...
	–145	$J = 1$	$16.00^{+1.50}_{-0.60}$	“	244 $^{+170}_{-170}$
2	2.42491(7)	$J = 0$	$14.60^{+0.10}_{-0.30}$	$1.3^{+1.7}_{-0.4}$...
	–121	$J = 1$	$15.00^{+0.05}_{-0.50}$	“	134 $^{+229}_{-69}$
		$J = 2$	$14.30^{+0.10}_{-0.20}$	“	223 $^{+149}_{-51}$
		$J = 3$	$15.30^{+0.30}_{-0.10}$	“	324 $^{+133}_{-41}$
		$J = 4$	$14.55^{+0.10}_{-0.20}$	“	422 $^{+54}_{-62}$
		$J = 5$	$14.30^{+0.20}_{-0.20}$	“	433 $^{+57}_{-45}$
		$J = 6$	<13.80	“	≤ 607
		$J = 7$	<13.70	“	≤ 648
	2.42659(1)	$J = 0$	$17.30^{+0.20}_{-0.60}$	$2.1^{+0.9}_{-1.0}$...
	+25	$J = 1$	$17.70^{+0.10}_{-0.30}$	“	134 $^{+63}_{-63}$
9	2.42688(5)	$J = 0$	$16.50^{+0.90}_{-0.50}$	“	148 $^{+47}_{-47}$
	+51	$J = 1$	$16.70^{+0.75}_{-0.50}$	“	231 $^{+546}_{-62}$
		$J = 2$	$16.70^{+0.75}_{-0.50}$	“	200 $^{+64}_{-22}$
		$J = 3$	$14.55^{+0.30}_{-0.25}$	“	≤ 264
		$J = 4$	$14.55^{+0.30}_{-0.25}$	“	≤ 361
		$J = 5$	≤ 14.00	“	≤ 361
		$J = 6$	<13.50	“	≤ 446
		$J = 7$	<13.70	“	≤ 446
	2.42713(5)	$J = 0$	$17.30^{+0.20}_{-0.60}$	$1.9^{+1.1}_{-0.4}$...
	+73	$J = 1$	$17.90^{+0.20}_{-0.20}$	“	209 $^{+111}_{-111}$
10	2.42729(3)	$J = 0$	$17.40^{+0.20}_{-0.40}$	“	371 $^{+186}_{-186}$
		$J = 1$	$17.00^{+0.30}_{-0.50}$	“	274 $^{+341}_{-83}$
		$J = 2$	$14.85^{+0.30}_{-0.35}$	“	218 $^{+78}_{-30}$
		$J = 3$	≤ 14.00	“	≤ 264
		$J = 4$	<13.50	“	≤ 361
		$J = 5$	<13.70	“	≤ 446
	2.42729(3)	$J = 0$	$14.95^{+0.10}_{-0.05}$	$2.5^{+1.0}_{-1.0}$...
	+87	$J = 1$	$15.35^{+0.05}_{-0.10}$	“	134 $^{+29}_{-35}$
		$J = 2$	$14.90^{+0.10}_{-0.30}$	“	297 $^{+74}_{-103}$
		$J = 3$	$15.10^{+0.10}_{-0.20}$	“	379 $^{+56}_{-77}$
12	2.42729(3)	$J = 4$	$14.20^{+0.10}_{-0.30}$	“	435 $^{+42}_{-83}$
		$J = 5$	≤ 13.70	“	≤ 408
	2.42729(3)	$J = 0$	$14.65^{+0.05}_{-0.10}$	$2.0^{+1.0}_{-1.0}$...
	+87	$J = 1$	$15.35^{+0.10}_{-0.30}$	“	291 $^{+1075}_{-169}$
		$J = 2$	$15.00^{+0.10}_{-0.35}$	“	637 $^{+855}_{-340}$
		$J = 3$	$15.20^{+0.10}_{-0.30}$	“	576 $^{+201}_{-180}$
13	2.42729(3)	$J = 4$	$14.10^{+0.10}_{-0.30}$	“	493 $^{+76}_{-93}$
		$J = 5$	≤ 13.70	“	≤ 469

¹ Velocity relative to $z_{\text{abs}} = 2.42630$.² Best fit values with errors representing the allowed range on $\log N(\text{H}_2)$, not the rms error on the fit. Due to the large uncertainties, only a range is given for component 1 (see text).³ Temperatures corresponding to the best-fit values. In some cases, the upper-limit on the ratio $N(\text{H}_2, J)/N(\text{H}_2, J = 0)$ is higher than the maximum expected ratio in case of local thermal equilibrium (see Eq. (1)), and the corresponding upper-limit on T_{0-J} doesn't exist.

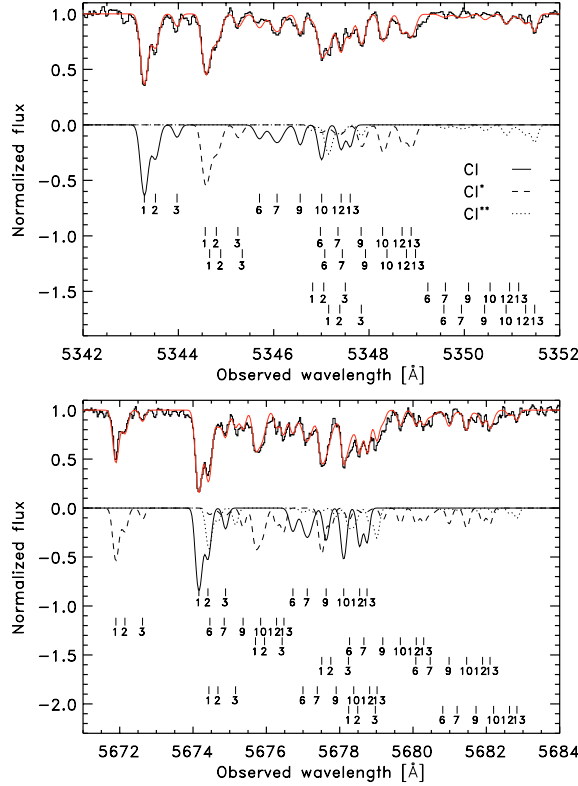


Fig. 2. Observed portions of the normalised spectrum of Q 2348–011 (upper part in both panels) where C I absorptions are seen, with the model spectrum superimposed. The model spectrum is decomposed into C I (solid line), C I* (dashed line), and C I** (dotted line) model spectra (lower part in both panels). The positions of the nine components are marked by small vertical lines. The associated labels correspond to the numbering in Table 3 (see also Tables 2 and 4).

3.1.2. Comments on individual components

Components 1 and 2, $z_{\text{abs}} = 2.42449(7)$ and $2.42463(8)$: these two components are heavily blended and appear as a single saturated feature for low H_2 rotational levels, but are better separated for $J \geq 4$, in C I and low-ionisation metal lines (see Figs. 2, 3 and 13). Doppler parameters, b , are mainly constrained by the H_2 L0–0 R0, H₂ L1–0 P2, H₂ L1–0 P3 profiles, and the transitions from the $J \geq 4$ rotational levels, but they remain uncertain. No damping wing is present. The first guess to fit the H_2 profiles, using redshifts from C I, C I*, and C I** transitions, was extremely helpful in this case. It must be emphasised that the blends of the two components can be fitted using either low b values, leading to high column densities or higher b values, leading to lower column densities. The best fit is obtained, however, with $b = 2.9 \text{ km s}^{-1}$ and column densities $\log N(H_2, J) = 17.15; 17.70; 17.00; 17.60; 15.40$ and 15.10 for $J = 0$ to $J = 5$, respectively. These are the values we use in the following. Rotational levels are unambiguously detected up to $J = 5$. Possible absorptions from $J = 6$ and $J = 7$ levels, unfortunately, are always redshifted on top of strong H I Lyman- α features or in regions of low SNR. Upper limits are given in Table 2.

Component 3, $z_{\text{abs}} = 2.42491(7)$: this component is the weakest in the system and is not saturated. The Doppler parameter is therefore mainly constrained by the strongest transition lines that are not blended: H₂ L2–0 R0, H₂ L1–0 R0, and H₂ L3–0 P1. Only the first four rotational levels are detected. $J = 3$ lines are always blended. However, the column-density can still be

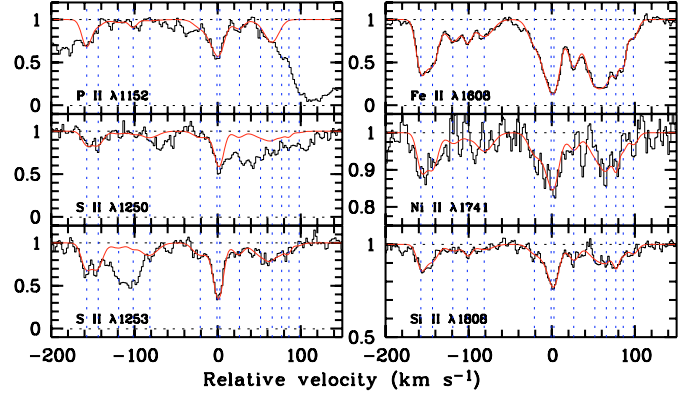


Fig. 3. Low-ionisation metal transitions in the $z_{\text{abs}} = 2.43$ DLA toward Q 2348–011. Note that the strongest component in the metal profiles (at $v = 0 \text{ km s}^{-1}$) does not show associated H_2 absorption (see Fig. 4). We give upper-limits on $N(P \text{ II})$ for the three redder components of P II as they are blended with intervening H I absorptions. S II transitions are also located in the Ly- α forest; but with the help of the two transitions shown above, we can still derive column densities or upper-limits for each component. Corresponding Voigt-profile parameters are given in Table 4.

estimated using H_2 L1–0 R3 (left-half of the profile), H_2 L1–0 P3, and H_2 L0–0 R3 (see Fig. 12).

Components 9 & 10, $z_{\text{abs}} = 2.42659(1)$ and $2.42688(5)$: These components have high H_2 column densities. They are separated well and Doppler parameters are constrained well by the width of the isolated and non-saturated absorption features H_2 L0–0 R0, H_2 L0–0 R1 and mostly of the P-branch ($\Delta J = -1$) Lyman-band transitions from the $J = 2$ to $J = 4$ rotational levels. Note that component 9 of a particular transition is often blended with components 1 and 2 of another transition from the next rotational level (see e.g., H_2 L2–0 R0 in Fig. 9). The first five rotational levels ($J = 0$ to $J = 4$) are detected. Some consistent features are seen for $J = 5$ (see transitions H_2 L4–0 P5 and H_2 L2–0 R5 in Fig. 14). Upper-limits were derived as the largest value consistent with the observed spectrum for levels $J = 5$, $J = 6$, and $J = 7$.

Components 12 and 13, $z_{\text{abs}} = 2.42713(5)$ and $2.42729(3)$: Absorptions from rotational levels $J = 0$ to $J = 4$ are detected in the two components. $N(J = 2)$ is constrained mainly by H_2 L0–0 P2, but the maximum N -value is also constrained by H_2 L3–0 R2 and H_2 L1–0 P2, whereas the minimum N -value is constrained by the local depth of the features clearly seen in H_2 L1–0 R2 and H_2 L0–0 R2 (see Fig. 11). Similar constraints are used for $J = 3$. $J = 4$ lines are blended or located in poor SNR regions, but we can still constrain the column-density thanks to H_2 L4–0 R4, H_2 L4–0 P4 and H_2 L3–0 P4. The $J = 5$ rotational levels may be detected; but the corresponding column densities are very uncertain, and one should probably consider these values only as upper limits (see Table 2).

A summary of the transitions used to constrain the column-density for each H_2 -component in a given rotational level is given in Table 1. The lines in this table are non-blended and have a rather good SNR, except when marked by “u” or “l” indicating that the line is used to estimate, respectively, an “upper” or a “lower” limit.

3.2. Neutral carbon

Neutral carbon is detected in nine components. The corresponding absorption profiles are complex, as resulting

Table 3. Column densities of the C I fine-structure levels.

#	z_{abs}	b [km s ⁻¹]	$\log N(\text{C I})$	$\log N(\text{C I}^*)$	$\log N(\text{C I}^{**})$ ¹	$\Delta v_{\text{C}_1/\text{H}_2}$ ^{2,3} [km s ⁻¹]	$\log N(\text{C I}^*)/N(\text{C I})$	$\log N(\text{C I}^{**})/N(\text{C I})$
1	2.42450(5)	4.2 ± 0.3	13.55 ± 0.02	13.51 ± 0.03	13.10 ± 0.04	+0.7	-0.04 ± 0.04	-0.45 ± 0.04
2	2.42465(4)	4.6 ± 0.4	13.10 ± 0.06	13.06 ± 0.02	12.54 ± 0.10	+1.4	-0.04 ± 0.06	-0.56 ± 0.12
3	2.42494(4)	2.8 ± 0.4	12.55 ± 0.08	12.66 ± 0.09	12.60 ± 0.12	+2.4	0.11 ± 0.12	0.05 ± 0.14
6	2.42605(3)	5.9 ± 0.5	12.70 ± 0.07	12.50 ± 0.09	<12.50	–	-0.20 ± 0.11	<–0.20
7	2.42628(9)	8.4 ± 0.5	12.96 ± 0.04	12.75 ± 0.04	<12.50	–	-0.21 ± 0.06	<–0.46
9	2.42660(0)	4.0 ± 0.5	12.80 ± 0.02	12.93 ± 0.10	<12.50	+0.8	0.13 ± 0.10	<–0.30
10	2.42688(9)	4.0 ± 0.5	13.09 ± 0.02	13.05 ± 0.04	12.55 ± 0.20	+0.3	-0.04 ± 0.04	-0.54 ± 0.20
12	2.42715(1)	3.2 ± 0.5	12.87 ± 0.04	12.84 ± 0.04	12.53 ± 0.05	+1.4	-0.03 ± 0.06	-0.34 ± 0.06
13	2.42727(3)	3.0 ± 0.6	12.80 ± 0.05	12.90 ± 0.03	12.80 ± 0.10	-1.7	0.10 ± 0.06	0.00 ± 0.11

¹ 3σ upper-limits are derived for $N(\text{C I}^{**})$ in components 6, 7 and 9.

² We estimate the errors on $\Delta v_{\text{C}_1/\text{H}_2}$ to be about 2 to 3 km s⁻¹.

³ There is no velocity shift between the components of neutral carbon and those of molecular hydrogen.

from the blend of absorption lines from three fine-structure levels of the neutral carbon ground state ($2s^2 2p^2 3P_{0,1,2}$). In Fig. 2 we show the fit to the C I absorption features around $\lambda_{\text{obs}} \approx 5346$ Å and $\lambda_{\text{obs}} \approx 5676$ Å with contributions from the eleven transitions: C I $\lambda\lambda 1560$, C I $\lambda 1656$, C I^{*} $\lambda\lambda 1560.6, 1560.7$, C I^{*} $\lambda\lambda\lambda 1656, 1657.3, 1657.9$, C I^{**} $\lambda\lambda 1561.3, 1561.4$, and C I^{**} $\lambda\lambda 1657, 1658$. We first performed a fit with seven C I components corresponding to the seven H₂ detected components, but we left the exact positions of the C I components free. We then added C I^{*}, and finally C I^{**} transitions. To reproduce the overall profile well, we had to introduce two weak C I components (#6 and 7) that are not detected in H₂, but are detected in the absorption profiles of low-ionisation metals. We then performed a second fit with nine components, in the same order: first C I only, then adding C I^{*} and finally C I^{**}. Finally all transitions were fitted together. The resulting small velocity shifts between C I and H₂ components (see Table 3) are within uncertainties. This means that H₂ and C I absorptions are generally produced in the same regions. Note, however, that the Doppler parameters found for the C I components are slightly larger than those found for the H₂ components, indicating that the C I regions are probably of slightly larger dimensions. Results of the fit (Fig. 2) are presented in Table 3. Three σ upper-limits are derived for $N(\text{C I}^{**})$ in components 6, 7, and 9, leading to upper-limits on $N(\text{C I}^{**})/N(\text{C I})$ (see Table 3).

3.3. Metal content

The absorption profiles of low-ionisation species (P II, S II, Fe II, Ni II and Si II) are complex and span about $\Delta v \approx 300$ km s⁻¹ in velocity space. Fourteen components were needed to reconstruct the whole profiles, i.e., the nine C I components plus five components that are not detected in C I. A few profiles are shown in Fig. 3 and results from the fit are given in Table 4. The overall metallicity is found to be -0.80 , -0.62 , and -1.17 ± 0.10 for, respectively, [Si/H], [S/H], and [Fe/H]. The strongest component (#7) in these profiles does not correspond to any H₂ component and is associated with a weak C I component. Redshifts have been relaxed to allow for the best fit to be obtained. Shifts between singly ionised metals components and C I components are well within errors, however. Voigt-profile parameters given in Table 4 are well-constrained for species with transitions located outside the Ly- α forest, i.e. Fe II, Ni II, and Si II. The S II and P II transitions are partly blended with intervening Ly- α H I absorptions. Nevertheless, all S II components can be constrained thanks to the observations of two different transitions. The three

redder components of P II are blended, and we cannot derive N(P II) for these components (see Table 4).

Figure 4 shows the overall absorption profile of highly ionised species: C IV and Si IV. It can be seen that the C IV counterpart of H₂ components are generally weak compared to the other components. The strongest C IV feature at $v = 0$ km s⁻¹ does not correspond to any H₂ component but corresponds to the strongest component in Fe II.

The iron-to-sulfur abundance ratio is plotted in Fig. 5 as a function of the silicon-to-sulfur abundance ratio. The abundance ratios are defined as $[\text{X/S}] = \log N(\text{X})/N(\text{S})_{\text{obs}} - \log N(\text{X})/N(\text{S})_{\odot}$. A strong correlation between [Fe/S] and [Si/S] is observed, similar to what has been observed previously by Petitjean et al. (2002) and Rodríguez et al. (2006). This correlation is easily interpreted as a depletion pattern of Fe and Si onto dust grains. Note that H₂ is detected in components where iron is not strongly depleted with [Fe/S] as high as -0.1 in component #10 and that the highest depletions are found in components where H₂ is not detected, components #5 and 8. However, components #7 and #8 are heavily blended and the distribution of N(S II) between these two components is uncertain. If we consider these two components as a single feature, then the corresponding depletion would be lower than for component #8. In component #5, the S II column-density might be overestimated due to poor SNR and a small blend (see Fig. 3). In addition, it can be seen in Fig. 3 that component #10 is blended in the wing of component #11. Therefore the decomposition is difficult, and the N(Fe II) column density in this component could be overestimated.

The typical abundance patterns in the Galactic halo, warm disk clouds, and cold disk clouds are also indicated in Fig. 5. As for Magellanic clouds, the halo pattern represents the depletion in individual DLA components best.

3.4. Chlorine

When H₂ is optically thick, singly-ionised chlorine (Cl II) will go through rapid charge exchange reaction with H₂ to produce H I and Cl I (see Jura 1974a). Neutral chlorine should therefore be a good tracer of H₂ (Jura & York 1978) and provide additional information for constraining the physical parameters of the gas. Unfortunately, the wavelength at which the strongest chlorine line (Cl I $\lambda 1347$) is expected to fall is not covered by our spectrum. It is possible to give an upper-limit on $N(\text{Cl I})$, thanks to Cl I $\lambda\lambda 1088$ and Cl I $\lambda\lambda 1101$ transitions whose oscillator strengths have recently been measured by Sonnentrucker et al. (2006). We derive $N(\text{Cl I}) \leq 10^{13}$ cm⁻² for each component at

Table 4. Results of the Voigt-profile fitting of the singly-ionised metal lines.

#	z_{abs}	Ion (X)	$\log N(X)$	b [km s $^{-1}$]	$\Delta v_{X/\text{Cl}}$ [km s $^{-1}$]
1	2.42450(5) -157	P II	12.84 ± 0.03	6.6 ± 0.1	+0.0
		S II	14.11 ± 0.02	“	
		Fe II	13.73 ± 0.01	“	
		Ni II	12.86 ± 0.05	“	
		Si II	14.30 ± 0.03	“	
2	2.42465(7) -144	P II	12.22 ± 0.09	8.1 ± 0.2	+0.3
		S II	14.21 ± 0.02	“	
		Fe II	13.70 ± 0.01	“	
		Ni II	12.92 ± 0.04	“	
		Si II	14.18 ± 0.04	“	
3	2.42494(4) -119	P II	11.97 ± 0.18	10.7 ± 0.7	+0.0
		S II	<13.60	“	
		Fe II	13.39 ± 0.01	“	
		Ni II	<12.50	“	
		Si II	13.87 ± 0.08	“	
4	2.42514(4) -101	P II	12.15 ± 0.09	5.1 ± 0.1	–
		S II	<13.60	“	
		Fe II	13.11 ± 0.01	“	
		Ni II	<12.50	“	
		Si II	13.82 ± 0.07	“	
5	2.42536(8) -82	P II	11.68 ± 0.48	13.5 ± 0.2	–
		S II	≤14.04	“	
		Fe II	13.35 ± 0.01	“	
		Ni II	12.81 ± 0.07	“	
		Si II	13.85 ± 0.09	“	
6	2.42605(6) -21	P II	12.32 ± 0.09	9.8 ± 0.2	+0.3
		S II	13.85 ± 0.05	“	
		Fe II	13.34 ± 0.01	“	
		Ni II	12.71 ± 0.08	“	
		Si II	13.93 ± 0.07	“	
7	2.42628(8) -1	P II	13.09 ± 0.04	11.9 ± 0.3	-0.1
		S II	14.08 ± 0.07	“	
		Fe II	14.10 ± 0.01	“	
		Ni II	13.18 ± 0.06	“	
		Si II	14.55 ± 0.04	“	
8	2.42632(7) +2	P II	12.45 ± 0.12	5.7 ± 0.1	–
		S II	14.49 ± 0.03	“	
		Fe II	13.58 ± 0.01	“	
		Ni II	<12.50	“	
		Si II	14.14 ± 0.08	“	
9	2.42660(0) +26	P II	12.35 ± 0.06	7.4 ± 1.0	+0.0
		S II	13.78 ± 0.06	“	
		Fe II	13.68 ± 0.01	“	
		Ni II	12.55 ± 0.09	“	
		Si II	14.12 ± 0.04	“	
10	2.42688(8) +51	P II	12.00 ± 0.03	12.0 ± 2.2	-0.1
		S II	13.90 ± 0.05	“	
		Fe II	14.09 ± 0.05	“	
		Ni II	12.81 ± 0.07	“	
		Si II	14.20 ± 0.15	“	
11	2.42705(4) +66	P II	12.90 ± 0.05	10.5 ± 3.5	–
		S II	14.04 ± 0.05	“	
		Fe II	13.92 ± 0.04	“	
		Ni II	12.97 ± 0.05	“	
		Si II	14.23 ± 0.05	“	
12	2.42718(3) +77	P II	blend	2.8 ± 1.5	+2.8
		S II	<13.60	“	
		Fe II	13.38 ± 0.01	“	
		Ni II	12.53 ± 0.08	“	
		Si II	13.97 ± 0.04	“	
13	2.42727(9) +86	P II	blend	3.4 ± 1.3	+0.5
		S II	<13.60	“	
		Fe II	13.47 ± 0.01	“	
		Ni II	<12.50	“	
		Si II	13.68 ± 0.08	“	
14	2.42741(5) +98	P II	blend	6.4 ± 1.2	–
		S II	<13.60	“	
		Fe II	13.14 ± 0.01	“	
		Ni II	<12.50	“	
		Si II	13.86 ± 0.06	“	

¹ Relative velocity (in km s $^{-1}$) to the center of the Lyman- α absorption at $z_{\text{abs}} = 2.42630$.

Upper-limits are given at 3σ , except in the case of S II in component 5, for which the column-density derived has been considered as an upper-limit to take account of a possible blend.

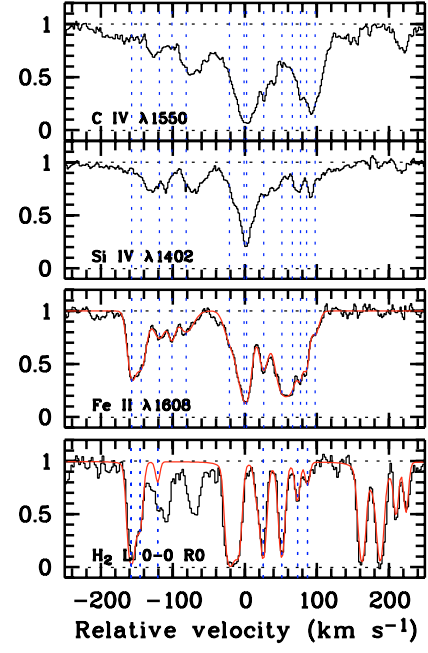


Fig. 4. Absorption profiles of Si IV and C IV in the $z_{\text{abs}} = 2.43$ DLA toward Q 2348–011. The vertical lines mark the positions of low-ionisation metal components in the C IV Si IV and Fe II panels. They mark the positions of the seven H₂ components in the H₂ L0–R0 panel.

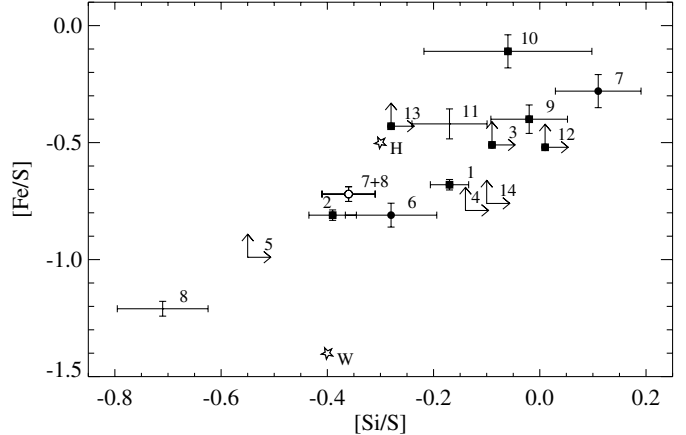


Fig. 5. The iron-to-sulfur abundance ratio, [Fe/S], is plotted as a function of the silicon-to-sulfur abundance ratio, [Si/S]. The observed correlation is interpreted as the result of depletion of Fe and Si onto dust grains. Different velocity components are numbered from 1 to 14. Filled squares are for components where both H₂ and Cl I are detected, while filled circles are for components where Cl I is detected but not H₂. The open circle stands for components 7 and 8 considered as a single velocity component. Stars mark the typical depletions observed in the Galactic halo clouds (H) and in clouds of the Galactic warm disk (W; see Table 6 of Welty et al. 1999). The point corresponding to the depletion in clouds of the Galactic cold disk would be located off of the graph with [Si/S] = -1.3 and [Fe/S] = -2.2.

the 3σ detection limit. This leads to about $N(\text{Cl I})/N(\text{H}_2) \leq 10^{-5}$ for the strongest H₂ components (1, 9, and 10). Typical ratios measured along lines of sight toward the Magellanic clouds and the Galactic disk are, respectively, $N(\text{Cl I})/N(\text{H}_2) \sim 0.4\text{--}3 \times 10^{-6}$ (André et al. 2004) and $N(\text{Cl I})/N(\text{H}_2) \sim 0.4 \times 10^{-6}$ (Sonnentrucker et al. 2002). The non-detection of Cl I with such an upper-limit is therefore not surprising. Singly-ionised chlorine (Cl II), in turn, has only two transitions at $\lambda_{\text{rest}} \simeq 1063$ Å and

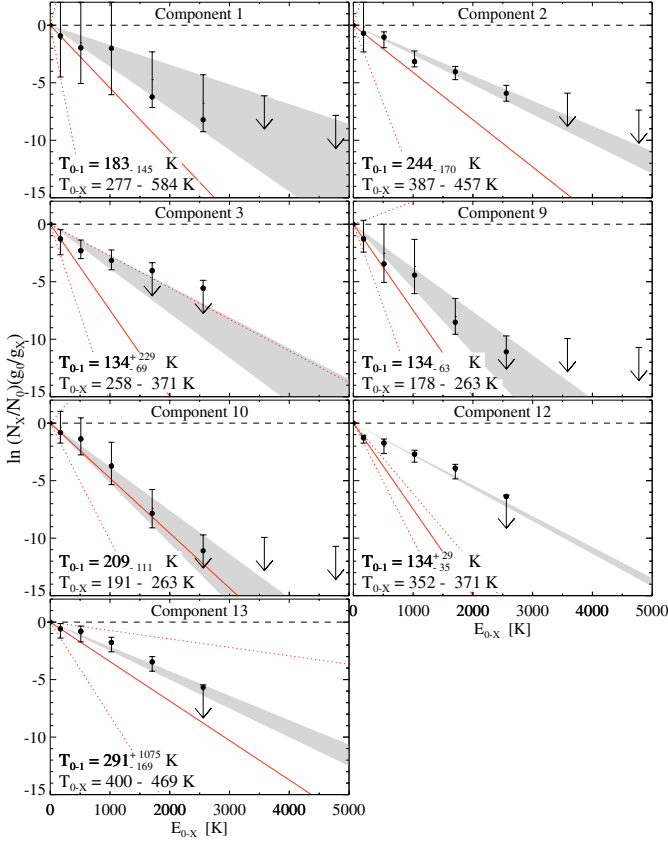


Fig. 6. Excitation diagrams for the seven H_2 components. The grey area shows the range of excitation temperatures that can explain the populations of the $J \geq 2$ rotational levels. The slope of straight lines give directly $1/T_{0-X}$. The solid line stands for T_{0-1} and dashed lines for the upper and lower limits on T_{0-1} .

1071 Å. The corresponding features are blended with H_2 or $\text{Ly}-\alpha$ lines, but an upper-limit at 3σ of about $N(\text{Cl II}) \leq 10^{14} \text{ cm}^{-2}$ can still be derived for components with a relative velocity between $v \approx -120 \text{ km s}^{-1}$ and -30 km s^{-1} (i.e. components 3, 4, and 5).

4. Determination of physical parameters

4.1. Excitation temperatures

The excitation temperature T_{XY} between two rotational levels X and Y is defined as

$$\frac{N_Y}{N_X} = \frac{g_Y}{g_X} e^{-E_{XY}/kT_{XY}} \quad (1)$$

where g_X is the statistical weight of rotational level X : $g_X = (2J_X + 1)(2I_X + 1)$ with nuclear spin $I = 0$ for even J (para- H_2) and $I = 1$ for odd J (ortho- H_2), k is the Boltzman constant, and E_{XY} is the energy difference between the levels $J = X$ and $J = Y$. If the excitation processes are dominated by collisions, then the populations of the rotational levels follow a Boltzman distribution described by a unique excitation temperature for all rotational levels. In Fig. 6, we plot, for each H_2 component, the natural logarithm of the ratios $N(\text{H}_2, J = X)/N(\text{H}_2, J = 0)$ weighted by the degeneracy factor g_X/g_0 against the energy between rotational levels. The slope of a straight line starting at the origin gives the inverse of the excitation temperatures T_{0-X} directly.

Figure 6 and Table 2 show that T_{0-1} is generally much lower than the other excitation temperatures. Generally, T_{0-1} is a good

indicator of the kinetic temperature (Roy et al. 2006; Le Petit et al. 2006). However, two effects could act, in opposite directions, against this simple assumption. If the $J = 1$ level is not thermalised, then T_{01} is a lower-limit on T_{kin} . On the contrary, the selective self-shielding of molecular hydrogen in the $J = 1$ level for column densities below $N(\text{H}_2) \approx 10^{16} \text{ cm}^{-2}$ should make T_{01} an upper-limit on T_{kin} . Given the large densities we derive in those components (see Sect. 4.3), collisions are not negligible and contribute towards thermalising the two levels. Despite large allowed ranges for individual components, and a relatively large dispersion among the individual components, the ratios $N(\text{H}_2, J = 1)/N(\text{H}_2, J = 0)$ for the seven H_2 components are all consistent with $T_{01} \approx 140 \text{ K}$, which corresponds to the intersection of all the individual T_{01} ranges. This value can be taken as representative of the kinetic temperature for the derivation of the densities (see Sect. 4.3). The kinetic temperatures, roughly estimated by T_{01} (see Table 2), are nevertheless similar to what was found in previous studies. Srianand et al. (2005), using the ortho-to-para ratio for thirteen H_2 components in seven DLAs, found $T \approx 153 \pm 78 \text{ K}$ (see also Ledoux et al. 2006b, $T \sim 90$ –180 K). These values are higher than those measured in the ISM ($77 \pm 17 \text{ K}$; Rachford et al. 2002) and in the Magellanic Clouds ($82 \pm 21 \text{ K}$; Tumlinson et al. 2002). On the other hand, they are similar to what is observed through high-latitude Galactic sight lines ($124 \pm 8 \text{ K}$; Gillmon et al. (2006) or ranging from 81 K at $\log N(\text{H}_2) = 20$ to 219 K at $\log N(\text{H}_2) = 14$; Wakker (2006)). This could be due to a high UV radiation field but also to different grain properties. Indeed, the photo-electric heating of the medium should be more efficient in the case of smaller grains. The higher excitation temperatures measured for higher rotational levels ($J \geq 2$) show that other processes than collisions are in play. Rotational levels $J = 4$ and $J = 5$ can be populated by cascades following UV or formation pumping. We indeed assume in the following that these are the main processes populating high- J levels. It is nevertheless also possible that the H_2 rotational excitation is due to C-shocks or turbulence (Joulain et al. 1998; Cecchi-Pestellini et al. 2005) as in diffuse clouds.

4.2. Photo-absorption rate

We can estimate the total absorption rate of Lyman- and Werner-band UV photons by H_2 in the $J = 0$ and $J = 1$ levels, β_0 and β_1 , respectively, following Jura (1975). The equilibrium of the $J = 4$ and 5 level populations is described by

$$p_{4,0} \beta_0 n(\text{H}_2, J = 0) + 0.19 R n(\text{H}) n = A_{4 \rightarrow 2} n(\text{H}_2, J = 4) \quad (2)$$

and

$$p_{5,1} \beta_1 n(\text{H}_2, J = 1) + 0.44 R n(\text{H}) n = A_{5 \rightarrow 3} n(\text{H}_2, J = 5) \quad (3)$$

where R is the H_2 molecule formation rate, n the proton density, p the pumping coefficients and A the spontaneous transition probabilities.

The factor 0.19 (resp. 0.44) means that about 19% (resp. 44%) of H_2 molecules form in the $J = 4$ (resp. $J = 5$) level (Jura 1974b). We use the spontaneous transition probabilities $A_{4 \rightarrow 2} = 2.8 \times 10^{-9} \text{ s}^{-1}$ and $A_{5 \rightarrow 3} = 9.9 \times 10^{-9} \text{ s}^{-1}$ (Spitzer 1978) and the pumping efficiencies $p_{4,0} = 0.26$ and $p_{5,1} = 0.12$ (Jura 1975). The pumping due to formation of molecules onto dust grains is often neglected if densities are lower than $5 \times 10^3 \text{ cm}^{-3}$, which is generally the case in damped Lyman- α systems (Srianand et al. 2005). However, in the following, we rewrite the above equations in a form that only depends on the relative populations of H_2 rotational levels.

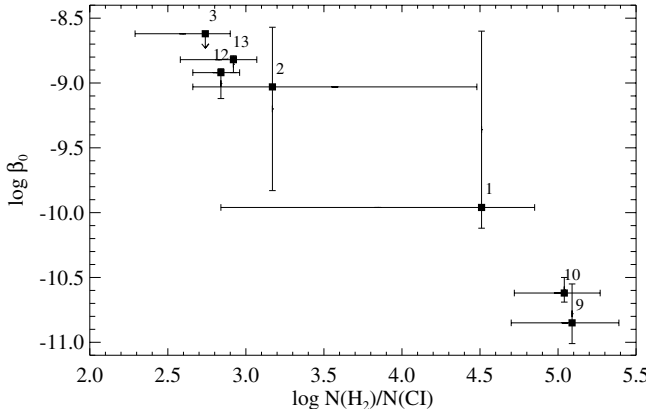


Fig. 7. Logarithm of the photo-absorption rate as a function of $\log N(\text{H}_2)/N(\text{CII})$. Squares stand for the best-fit values. Despite large allowed ranges on β_0 and $N(\text{H}_2)/N(\text{CII})$ (dominated by the $N(\text{H}_2)$ uncertainties), there is a clear anti-correlation between the two quantities.

The equilibrium between formation and destruction of H_2 can be written

$$R n n(\text{H}) = R_{\text{diss}} n(\text{H}_2) \quad (4)$$

where $R_{\text{diss}} = 0.11\beta_0$, assuming that 11% of the photo-absorptions lead to photo-dissociations (Jura 1974b).

We can substitute $R n n(\text{H})$ in Eqs. 2 and 3 and finally obtain (see also Cui et al. 2005):

$$p_{4,0}\beta_0 \frac{N(\text{H}_2, J=0)}{N(\text{H}_2)} + 0.021\beta_0 = A_{4 \rightarrow 2} \frac{N(\text{H}_2, J=4)}{N(\text{H}_2)} \quad (5)$$

and

$$p_{5,1}\beta_1 \frac{N(\text{H}_2, J=1)}{N(\text{H}_2)} + 0.049\beta_1 = A_{5 \rightarrow 3} \frac{N(\text{H}_2, J=5)}{N(\text{H}_2)}. \quad (6)$$

One advantage of these expressions is that $\beta_{0,1}$ can be determined in each component without any assumption to estimate $N(\text{H I})$ in the component. Values obtained for $\beta_{0,1}$ in the different components are given in Table 4, where it can be seen that the usual assumption $\beta_0 = \beta_1$ is verified.

We find the photo-absorption rate of H_2 in the Lyman and Werner bands $\beta_0 \in [7.6 \times 10^{-11}, 2.5 \times 10^{-9}] \text{ s}^{-1}$ ($\beta_0 \simeq 1.1 \times 10^{-10} \text{ s}^{-1}$ for the best-fit value) in component 1; $\beta_0 \simeq 1 \times 10^{-9} \text{ s}^{-1}$ in component 2; $\beta_0 \simeq 1.2 \times 10^{-9} \text{ s}^{-1}$ in component 12 and $\beta_0 \simeq 1.5 \times 10^{-9} \text{ s}^{-1}$ in component 13. Much lower values are found for components with higher H_2 column densities: for component 9 ($\beta_0 \simeq 1.4 \times 10^{-11} \text{ s}^{-1}$), and for component 10 ($\beta_0 \simeq 2.4 \times 10^{-11} \text{ s}^{-1}$). We also derive an upper-limit on the photo-absorption rate for components 3 ($\beta_0 \lesssim 2.4 \times 10^{-9} \text{ s}^{-1}$). These values are spread over about 2 orders of magnitude.

We plot the photo-absorption rate, β_0 , versus $\log N(\text{H}_2)/N(\text{CII})$ in Fig. 7. Srianand & Petitjean (1998) suggest that this latter ratio is a good indicator of the physical conditions in the absorber as it increases when the ionisation parameter decreases. There is an anti-correlation ($R = -0.97$) between $\log \beta_0$ and $\log N(\text{H}_2)/N(\text{CII})$ that is mostly due to shielding effects.

We can correct for the shielding effect (self-shielding and dust-shielding) and estimate the UV background intensity outside the cloud. The photo-dissociation rate is related to the ambient UV flux:

$$R_{\text{diss}} = 0.11\beta_0 = (4\pi) 1.1 \times 10^8 J_{\text{LW}} S_{\text{shield}} (\text{s}^{-1}) \quad (7)$$

where J_{LW} ($\text{erg s}^{-1} \text{cm}^{-2} \text{Hz}^{-1} \text{sr}^{-1}$) is the UV intensity at $h\nu = 12.87 \text{ eV}$, averaged over the solid angle (Abel et al. 1997; Hirashita & Ferrara 2005). The term S_{shield} is the correction factor for H_2 self-shielding (Draine & Bertoldi 1996) and dust extinction. For $\log N(\text{H}_2) > 14$, it can be expressed as

$$S_{\text{shield}} = \left(\frac{N(\text{H}_2)}{10^{14} \text{ cm}^{-2}} \right)^{-0.75} e^{-\sigma_d N_d}. \quad (8)$$

The term due to dust extinction, $e^{-\sigma_d N_d}$, is expressed using the optical depth of the dust in the UV, $\tau_{\text{UV}} \equiv \sigma_d N_d$:

$$\tau_{\text{UV}} = 0.879 \left(\frac{a}{0.1 \mu\text{m}} \right)^{-1} \left(\frac{\delta}{2 \text{ g cm}^{-3}} \right)^{-1} \left(\frac{\mathcal{D}}{10^{-2}} \right) \left(\frac{N_{\text{H}}}{10^{21} \text{ cm}^{-2}} \right) \quad (9)$$

where a is the radius of a grain, \mathcal{D} the dust-to-gas mass ratio, and δ the grain material density (Hirashita & Ferrara 2005). Given the low H I column density, the exponential term is always very close to 1, and $S_{\text{shield}} \simeq (N(\text{H}_2)/10^{14} \text{ cm}^{-2})^{-0.75}$; therefore,

$$J_{\text{LW}} \simeq \frac{8 \times 10^{-11} \beta_0}{S_{\text{shield}}}. \quad (10)$$

It can be seen in Table 5 that for each component, the allowed ranges for J_{LW} are all much smaller compared to the larger allowed ranges for β_0 . This is especially true for components 1 and 2 (see also Fig. 7) and caused by errors in N being correlated with errors in Doppler parameters. Since absorptions from the low J levels are more saturated than those from the higher J levels, the derived N are more sensitive to a change in b ; when b is decreased, $\log N(\text{high})/N(\text{low})$ decreases, and the derived value of β_0 gets lower but the shielding correction is larger. Therefore the J_{LW} values derived for extreme values of b (see Sect. 3.1.2 and Table 2) are similar.

The derived UV intensity is about one to two orders of magnitude higher than the typical Galactic UV intensity that is about $J_{\text{LW},\odot} \simeq 3.2 \times 10^{-20} \text{ erg s}^{-1} \text{cm}^{-2} \text{Hz}^{-1} \text{sr}^{-1}$ in the solar vicinity (Habing 1968). Using FUSE, Tumlinson et al. (2002) also derive in the Magellanic clouds UV fluxes 10 to 100 times higher than in the Milky Way. This can be interpreted as in-situ star-formation close to the absorbing clouds. Note that, after shielding correction, the scatter in J_{LW} is much smaller than the two orders of magnitude variation in β_0 from one component to the other. It must be recalled that this is derived under the assumption that high- J excitation is mainly due to UV pumping and formation on dust grains.

The observed ratio of the ambient UV flux to that in the solar vicinity, $\chi = J_{\text{LW}}/J_{\text{LW},\odot}$, is in the range $\chi \sim 30$ –300. This should be considered as upper limits, as no other excitation processes than UV pumping and formation on dust is considered here. In any case, the observed excitations are still higher than in the Galactic halo or the Magellanic clouds. We therefore safely estimate that the present UV flux is about one order of magnitude higher than in the ISM.

Using the relation between the star-formation rate (SFR) per unit surface and χ , $\Sigma_{\text{SFR}} = 1.7 \times 10^{-3} \chi M_{\odot} \text{ yr}^{-1} \text{kpc}^{-2}$ (Hirashita & Ferrara 2005), we derive a SFR in the different components in the range, $\Sigma_{\text{SFR}} \sim 5$ – $50 \times 10^{-2} M_{\odot} \text{ yr}^{-1} \text{kpc}^{-2}$. The detailed values are given in Table 5. It can be seen that there is a gradient in the SFR through the DLA profile. The derived SFR is higher close to component 1. Note that if the star-formation region is larger than about 1 kpc, the associated Lyman- α emission should be detectable (e.g. Møller et al. 2004; Heinmüller et al. 2006).

Table 5. UV radiation field and star-formation rate around individual components.

#	$\log \beta_0$ [s ⁻¹]	$\log \beta_1$ [s ⁻¹]	$\log J_{\text{LW}}$ [erg/s/cm ² /Hz/sr]	Σ_{SFR} [$M_{\odot}/\text{yr}/\text{kpc}^2$]
1	$-9.96^{+1.36}_{-0.16}$	$-9.96^{+1.10}_{-0.22}$	$-17.02^{+0.26}_{-0.13}$	51×10^{-2}
2	$-9.00^{+0.46}_{-0.80}$	$-9.03^{+0.29}_{-1.21}$	$-17.41^{+0.05}_{-0.14}$	21×10^{-2}
3	$\lesssim -8.62$	$\lesssim -8.23$	$\lesssim -17.74$	$\lesssim 9 \times 10^{-2}$
9	$-10.85^{+0.30}_{-0.16}$	< -10.67	$-18.01^{+0.35}_{-0.14}$	5×10^{-2}
10	$-10.62^{+0.12}_{-0.07}$	< -10.96	$-17.82^{+0.27}_{-0.02}$	8×10^{-2}
12	$-8.92^{+0.03}_{-0.20}$	< -9.03	$-17.70^{+0.08}_{-0.28}$	10×10^{-2}
13	$-8.82^{+0.03}_{-0.10}$	< -8.74	$-17.62^{+0.37}_{-0.30}$	13×10^{-2}

4.3. C I fine structure

Neutral carbon is usually seen in components where H₂ is detected. As the ionisation potential of C I (11.2 eV) is similar to the energy of photons in the Werner and Lyman bands, C I is usually a good tracer of the physical conditions in the molecular gas. In the present system, C I is detected in all components where H₂ is detected but is also detected in two additional components (#6 and 7). It is possible to derive constraints on the particle density of the gas from relative populations of the fine-structure levels of the C I ground term (2s²2p²3P_{0,1,2}). In Fig. 8 we compare the ratios $N(\text{C I}^*)/N(\text{C I})$ and $N(\text{C I}^{**})/N(\text{C I})$ with models computed with the code POPRATIO (Silva & Viegas 2001). Taking into account the cosmic microwave background (CMB) radiation with temperature $T_{\text{CMBR}} = 2.73 \times (1+z)$ and assuming an electron density of $n_e = 10^{-4} \times n_{\text{H}}$, kinetic temperatures in the range $T = 80$ –200 K, and radiative excitation similar to that in the Milky Way, we derive hydrogen densities of the order of $n(\text{H I}) \simeq 100$ –200 cm⁻³ for the components where H₂ is detected. It is in turn about $n(\text{H I}) \simeq 50$ cm⁻³ for components without H₂ detection if we assume the same kinetic temperature. If the temperature is higher in these two components (#6 and 7), then densities would be even lower. The results are hardly dependent on the exact value of the ambient flux and on the electron and H₂ densities for this range of particle densities. The most influential processes in that case are the radiative excitation from the CMB and the collisional excitation depending on $n(\text{H I})$ and T . To illustrate this, we also assumed an ambient flux 30 times higher than the Galactic flux. The above densities for components 6 and 7 are decreased by a factor of about 2 and even less for the other components. Note however, that a very high UV flux (~100 times the Galactic flux) would make the observed C I fine-structure column-density ratios inconsistent with the models for the lowest-density components. This again shows that the UV flux derived in the previous section is probably an upper-limit.

Assuming temperatures between $T \sim 80$ K and $T \sim 200$ K also gives very similar results. Using a Galactic ISM temperature of $T = 80$ K leads to a higher inconsistency between the $N(\text{C I}^*)/N(\text{C I})$ and $N(\text{C I}^{**})/N(\text{C I})$ ratios. This supports the idea already mentioned in the previous section that the kinetic temperature is higher in this system than in the Galactic ISM (see Figs. 6, 8 and Table 6). Note that, because the column densities $N(\text{C I}^{**})$ are close to the 3 σ detection-limit ($\log N(\text{C I}^{**}) = 12.50$) and rather dependent on the continuum placement, densities derived from $N(\text{C I}^*)/N(\text{C I})$ are the most reliable.

5. Discussion and conclusions

We have detected strong molecular hydrogen absorption lines associated with the DLA at $z_{\text{abs}} = 2.4263$ toward Q 2348–011 in

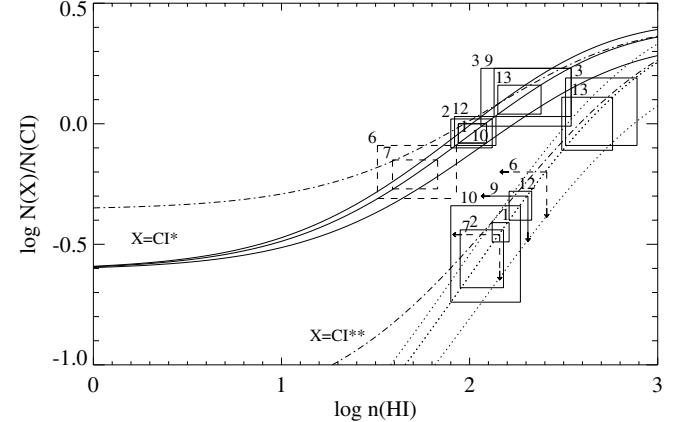


Fig. 8. Analysis of the C I fine-structure relative populations using results from the POPRATIO code (Silva & Viegas 2001). Solid and dashed lines give, respectively, $N(\text{C I}^*)/N(\text{C I})$ and $N(\text{C I}^{**})/N(\text{C I})$ versus gas density for a Galactic ambient flux. The corresponding thick lines stand for the model with $T = 140$ K, whereas the thin lines stand for $T = 200$ K (upper curves) and $T = 80$ K (lower curves). The dashed-dotted lines represent the model with an ambient flux 30 times higher than the Galactic flux. Boxes show the observed 1 σ range vertically for $N(\text{C I}^*)/N(\text{C I})$ and $N(\text{C I}^{**})/N(\text{C I})$ and horizontally the corresponding n values for the model with Galactic ambient flux and $T = 140$ K. They are therefore arbitrarily centred on the corresponding curve. Note that the results from different models are within errors. The influence of the UV flux is higher for components 6 and 7, for which no H₂ has been found. The corresponding derived densities are therefore considered as upper limits.

Table 6. Densities derived using models in Fig. 8 with $T = 140$ K, and the ratios $N(\text{C I}^*)/N(\text{C I})$ (Col. 2), $N(\text{C I}^{**})/N(\text{C I})$ (Col. 3).

#	$N(\text{C I}^*)/N(\text{C I})$	$n(\text{H I})$ [cm ⁻³]	adopted ¹
		$N(\text{C I}^{**})/N(\text{C I})$	
1	87–123	132–162	105 ± 18
2	79–132	89–151	106 ± 27
3	115–347	324–776	231 ± 116
6	32–85	<257	<59 ²
7	39–68	<145	<54 ²
9	135–347	<204	170 ± 35
10	87–123	79–186	105 ± 18
12	83–138	162–214	111 ± 28
13	141–240	309–575	191 ± 50

¹ Because $N(\text{C I}^*)$ is more reliable than $N(\text{C I}^{**})$, we take the corresponding n value as the actual n value (Col. 4), unless there is an upper limit on $N(\text{C I}^{**})$ that is then taken into account (component 9).

² The values for components 6 and 7 are considered as upper-limits, because of the higher dependence on the ambient UV flux.

seven velocity components spread over ~ 300 km s⁻¹ and from rotational levels $J = 0$ up to $J = 5$. We used these observations to constrain the physical conditions in the gas.

From the fine-structure levels of neutral carbon, we derived hydrogen volumic densities of the order of 100 to 200 cm⁻³ in the components where H₂ is detected. Densities below 50 cm⁻³ are derived in the two components where C I is detected but not H₂. This agrees with the results from Srianand et al. (2005). The relative populations of the first two rotational levels are all consistent with a kinetic temperature of about 120 to 160 K, under the assumption that T_{01} is a good indicator of T_{kin} . The temperatures derived are higher than typical temperatures in the ISM of the Galaxy. Detailed models of diffuse molecular clouds

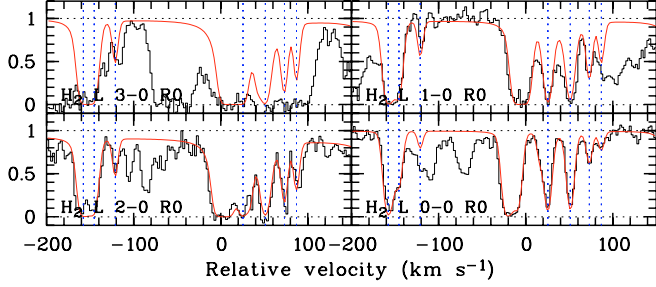


Fig. 9. H_2 rotational level $J = 0$. The centre of the velocity scale is set at $z_{\text{abs}} = 2.4263$. Continuum is seen depressed for $\text{H}_2 \text{L}2-0 \text{R}0$ and $\text{H}_2 \text{L}1-0 \text{R}0$ because of the $z_{\text{abs}} = 2.615$ Ly- β absorption. Components are marked by dashed lines. The strong absorptions at $v \sim -10 \text{ km s}^{-1}$ is due to $J = 1$ transition lines.

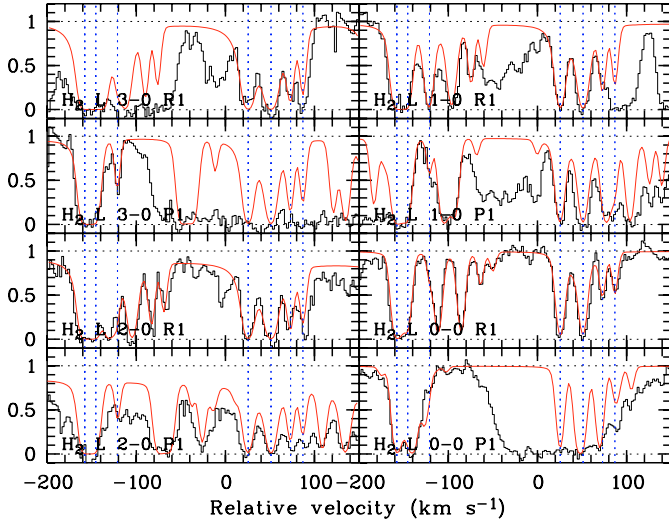


Fig. 10. H_2 rotational level $J = 1$. Continuum is depressed in panels $\text{H}_2 \text{L}2-0 \text{R}1$ to $\text{H}_2 \text{L}1-0 \text{R}1$ because of $z_{\text{abs}} = 2.615$ Ly- β absorption. The $J = 1$ components are marked by dashed lines, the other ones come from other transitions (in general $J = 0-2$).

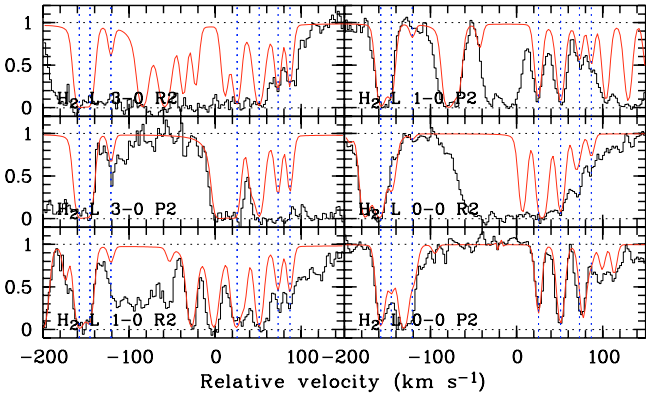


Fig. 11. H_2 rotational level $J = 2$. $\text{H}_2 \text{L}1-0 \text{P}2$ is blended with $\text{FeII}\lambda 1096$.

should be constructed to understand the origin of this difference. Actual kinetic temperatures could even be slightly higher if the $J = 1$ level is not thermalised (see, e.g., Le Petit et al. 2006), and then densities would also be slightly lower.

The physical properties of the H_2 -bearing gas are characteristic of a cold neutral medium. Molecular hydrogen in this DLA traces cold gas but with a higher pressure (of the order of $p \sim 10^4 \text{ cm}^{-3}\text{K}$) than that measured along lines of sight in the

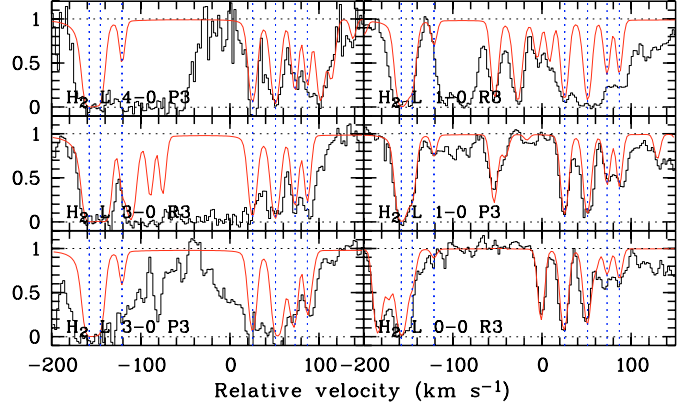


Fig. 12. H_2 rotational level $J = 3$. $\text{H}_2 \text{L}1-0 \text{R}3$ is blended with $\text{FeII}\lambda 1096$.

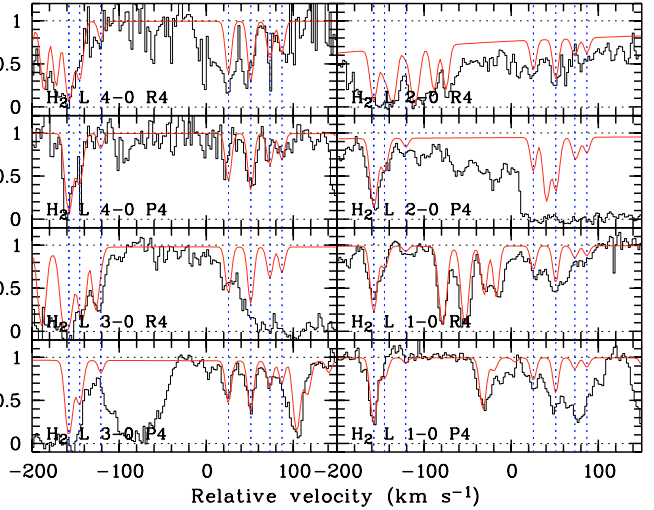


Fig. 13. H_2 rotational level $J = 4$. Continuum is depressed in some panels by $z_{\text{abs}} \simeq 2.6$ Ly- β absorption. The feature in the $\text{H}_2 \text{L}1-0 \text{P}4$ panel at $v \geq -50 \text{ km s}^{-1}$ might be due to CIV absorption at $z_{\text{abs}} \simeq 1.45$.

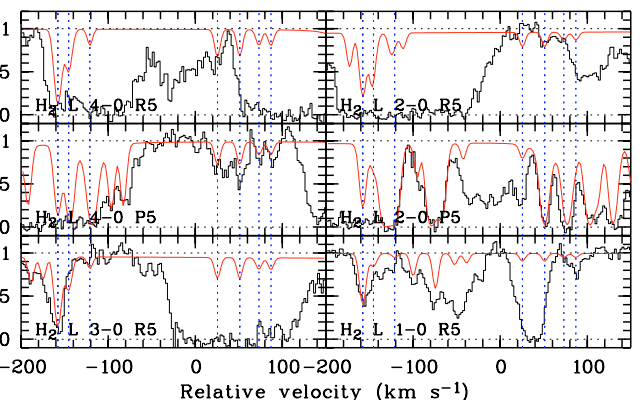


Fig. 14. H_2 rotational level $J = 5$. Most lines are blended with Ly- α or with $z_{\text{abs}} \simeq 1.45$ CIV absorptions. Column densities are mainly constrained by $\text{H}_2 \text{L}3-0 \text{R}5$ for components 1 and 2 and by $\text{H}_2 \text{L}4-0 \text{P}5$ (resp. $\text{H}_2 \text{L}2-0 \text{R}5$) for component 9 (resp. 10).

Galactic ISM. Temperatures and densities are similar to those observed in the Galactic halo (Wakker 2006; Richter et al. 2003).

If we assume that HI is distributed over the nine C I-bearing components proportionally to $N(\text{C I})$, then the mean HI column density is about $10^{19.5} \text{ cm}^{-2}$ in individual components. The

molecular clouds must therefore have an extension along the line of sight that is smaller than 1 pc. This supports the view that H₂-bearing gas is clumped into small clouds (see, e.g., Hirashita et al. 2003).

From the relative populations of H₂ rotational levels, we derived photo-absorption rates. Correcting for self-shielding, we are able to estimate the incident UV flux on the cloud, which we find to be about one order of magnitude higher than in the solar vicinity, similar to what is observed through the Magellanic clouds (Tumlinson et al. 2002). This shows that there is ongoing star formation in this system.

Searches for the galaxy responsible for the $z_{\text{abs}} = 2.4263$ DLA toward Q 2348–011 have been unsuccessful until now. Mannucci et al. (1998), using the NICMOS3 256² MAGIC camera at the Calar Alto 3.5 m telescope, reported the detection of an H α emission-line galaxy at $z \simeq 2.43$. The object is located at ~ 11 arcsec, corresponding to ~ 90 kpc for the standard Ω CDM cosmology, from the line of sight toward Q 2348–011 and the inferred SFR is $78 M_{\odot} \text{ yr}^{-1}$. The emission from the corresponding star-formation region is not large enough to explain the UV flux in which the gas is embedded. Bunker et al. (1999) spectroscopically observed Q 2348–011 over the wavelength range where possible H α emission at $z = 2.43$ would be redshifted. From the non-detection of any emission, they derived an upper limit of about $SFR \leq 21 h^{-2} M_{\odot} \text{ yr}^{-1}$ for the SFR of any possible object exactly aligned with the quasar. However, their observations are not very sensitive ($\sim 10^{-15} \text{ erg/s/cm}^2$). More recently Colbert & Malkan (2002) obtained coronographic H -band images of the field with the Near-Infrared Camera and Multi-Object Spectrograph mounted on the Hubble Space Telescope. With a 5σ detection limit $H = 22$, they detected three objects at 3.3, 9.7, and 10.7 arcsec or 19, 55, and 61 h^{-1} kpc from Q 2348–011. If at the same redshift as the DLA, these objects are about 1 to 2 mag brighter than an L_{*} galaxy. In particular the authors reject the object closer to the line of sight as a possible DLA galaxy candidate because of its brightness.

The origin of the UV excess in the vicinity of the gas is therefore unclear. Either one or several objects within 11 arcsec from the quasar are indeed at the redshift of the DLA and provide the inferred UV flux through star-formation activity or the region of star-formation is located on the line of sight to the quasar that is exactly aligned with it. In that case, Lyman- α emission should be observed at the bottom of the DLA trough. The SDSS spectrum of Q 2348–011 is too noisy to claim anything in this matter. It will thus be very interesting (i) to determine the spectroscopic redshifts of the objects that are located close to the line of sight and (ii) to perform deep intermediate-resolution spectroscopy of the quasar to search for any Lyman- α emission.

Acknowledgements. We thank the anonymous referee for a thorough reading of the manuscript and useful comments. P.N. is supported by a PhD fellowship from ESO. P.P.J. and R.S. gratefully acknowledge support from the Indo-French Centre for the Promotion of Advanced Research (Centre Franco-Indien pour la Promotion de la Recherche Avancée) under contract No. 3004-3.

References

Abel, T., Anninos, P., Zhang, Y., & Norman, M. L. 1997, *New Astron.*, 2, 181

Abgrall, H., Roueff, E., Launay, F., & Roncin, J. Y. 1993, *A&AS*, 101, 273

André, M. K., Le Petit, F., Sonnentrucker, P., et al. 2004, *A&A*, 422, 483

Ballester, P., Modigliani, A., Boitquin, O., et al. 2000, *The Messenger*, 101, 31

Bunker, A. J., Warren, S. J., Clements, D. L., Williger, G. M., & Hewett, P. C. 1999, *MNRAS*, 309, 875

Cecchi-Pestellini, C., Casu, S., & Dalgarno, A. 2005, *MNRAS*, 364, 1309

Colbert, J. W., & Malkan, M. A. 2002, *ApJ*, 566, 51

Cui, J., Bechtold, J., Ge, J., & Meyer, D. M. 2005, *ApJ*, 633, 649

Dekker, H., D'Odorico, S., Kaufer, A., Delabre, B., & Kotzlowski, H. 2000, in *Optical and IR Telescope Instrumentation and Detectors*, ed. M. Iye, & A. F. Moorwood, Proc. SPIE, 4008, 534

Draine, B. T., & Bertoldi, F. 1996, *ApJ*, 468, 269

Fynbo, J. P. U., Starling, R. L. C., Ledoux, C., et al. 2006, *A&A*, 451, L47

Ge, J., & Bechtold, J. 1999, in *Highly Redshifted Radio Lines*, ed. C. L. Carilli, S. J. E. Radford, K. M. Menten, & G. I. Langston, *ASP Conf. Ser.*, 156, 121

Gillmon, K., Shull, J. M., Tumlinson, J., & Danforth, C. 2006, *ApJ*, 636, 891

Greveste, N., & Sauval, A. J. 2002, *Adv. Space Res.*, 30, 3

Habing, H. J. 1968, *Bull. Astron. Inst. Netherlands*, 19, 421

Heinmüller, J., Petitjean, P., Ledoux, C., Caucci, S., & Srianand, R. 2006, *A&A*, 449, 33

Hirashita, H., & Ferrara, A. 2005, *MNRAS*, 356, 1529

Hirashita, H., Ferrara, A., Wada, K., & Richter, P. 2003, *MNRAS*, 341, L18

Jenkins, E. B., & Shaya, E. J. 1979, *ApJ*, 231, 55

Joulain, K., Falgarone, E., Des Forêts, G. P., & Flower, D. 1998, *A&A*, 340, 241

Jura, M. 1974a, *ApJ*, 190, L33

Jura, M. 1974b, *ApJ*, 191, 375

Jura, M. 1975, *ApJ*, 197, 581

Jura, M., & York, D. G. 1978, *ApJ*, 219, 861

Le Petit, F., Nehmé, C., Le Bourlot, J., & Roueff, E. 2006, *ApJS*, 164, 506

Ledoux, C., Srianand, R., & Petitjean, P. 2002, *A&A*, 392, 781

Ledoux, C., Petitjean, P., & Srianand, R. 2003, *MNRAS*, 346, 209

Ledoux, C., Petitjean, P., Fynbo, J. P. U., Møller, P., & Srianand, R. 2006a, *A&A*, 457, 71

Ledoux, C., Petitjean, P., & Srianand, R. 2006b, *ApJ*, 640, L25

Levshakov, S. A., Chaffee, F. H., Foltz, C. B., & Black, J. H. 1992, *A&A*, 262, 385

Mannucci, F., Thompson, D., Beckwith, S. V. W., & Williger, G. M. 1998, *ApJ*, 501, L11

Møller, P., Fynbo, J. P. U., & Fall, S. M. 2004, *A&A*, 422, L33

Morton, D. C. 2003, *ApJS*, 149, 205

Péroux, C., McMahon, R. G., Storrie-Lombardi, L. J., & Irwin, M. J. 2003, *MNRAS*, 346, 1103

Petitjean, P., Srianand, R., & Ledoux, C. 2002, *MNRAS*, 332, 383

Petitjean, P., Ledoux, C., Noterdaeme, P., & Srianand, R. 2006, *A&A*, 456, L9

Prochaska, J. X., Herbert-Fort, S., & Wolfe, A. M. 2005, *ApJ*, 635, 123

Rachford, B. L., Snow, T. P., Tumlinson, J., et al. 2002, *ApJ*, 577, 221

Reimers, D., Baade, R., Quast, R., & Levshakov, S. A. 2003, *A&A*, 410, 785

Richter, P., Wakker, B. P., Savage, B. D., & Sembach, K. R. 2003, *ApJ*, 586, 230

Rodríguez, E., Petitjean, P., Aracil, B., Ledoux, C., & Srianand, R. 2006, *A&A*, 446, 791

Roy, N., Chengalur, J. N., & Srianand, R. 2006, *MNRAS*, 365, L1

Sargent, W. L. W., Steidel, C. C., & Boksenberg, A. 1989, *ApJS*, 69, 703

Savage, B. D., Bohlin, R. C., Drake, J. F., & Budich, W. 1977, *ApJ*, 216, 291

Silva, A. I., & Viegas, S. M. 2001, *Comput. Phys. Commun.*, 136, 319

Sonnentrucker, P., Friedman, S. D., Welty, D. E., York, D. G., & Snow, T. P. 2002, *ApJ*, 576, 241

Sonnentrucker, P., Friedman, S. D., & York, D. G. 2006, *ApJ*, 650, L115

Spitzer, L. 1978, *Physical processes in the interstellar medium* (New York: Wiley-Interscience), 333

Srianand, R., & Petitjean, P. 1998, *A&A*, 335, 33

Srianand, R., Petitjean, P., Ledoux, C., Ferland, G., & Shaw, G. 2005, *MNRAS*, 362, 549

Tumlinson, J., Shull, J. M., Rachford, B. L., et al. 2002, *ApJ*, 566, 857

Wakker, B. P. 2006, *ApJS*, 163, 282

Welty, D. E., Frisch, P. C., Sonneborn, G., & York, D. G. 1999, *ApJ*, 512, 636

Wolfe, A. M., Turnshek, D. A., Smith, H. E., & Cohen, R. D. 1986, *ApJS*, 61, 249

Wolfe, A. M., Gawiser, E., & Prochaska, J. X. 2005, *ARA&A*, 43, 861